Research Article

Synthesis of a Novel Nanoparticle BaCoO$_{2.6}$ through Sol-Gel Method and Elucidation of Its Structure and Electrical Properties

Fareenpoornima Rafiq,[1] **Parthipan Govindsamy** ![ORCID],[1] **and Selvakumar Periyasamy** ![ORCID][2]

^{1}*Department of Physics, Vel Tech Multi Tech Dr. Rangarajan Dr. Sakunthala Engineering College, Chennai 600062, India*
^{2}*Department of Chemical Engineering, Adama Science and Technology University, Adama, Ethiopia*

Correspondence should be addressed to Parthipan Govindsamy; phdparthipan@gmail.com
and Selvakumar Periyasamy; selvakumar.periyasamy@astu.edu.et

The physical properties of cobalt oxide with varied oxidation states, and coordination numbers, in the transition series, have numerous applications. The present study explores the physical properties of BaCoO$_{2.6}$ nanoparticles synthesized through the sol-gel method. The X-ray diffraction figure exhibits a 25 nm crystallite size hexagonal phase. The observational data shows the reduction in the real part of impedance ($Z^{'}$), dielectric constant ($\xi^{'}$), dielectric loss ($\xi^{''}$), and a raise in ac conductivity of mixed type of conduction with an elevation in frequency analyzed through impedance spectroscopy. The conductivity due to grain and grain boundaries is shown foremost in the complex impedance analysis. The plot of $\Delta V/\Delta T$ (Seebeck coefficient) in the low-temperature range indicates p-type behavior and the metal-insulator transition in the as-synthesized sample. The sample characteristics suggest applications in optical and switching devices. The Seebeck coefficient is the generation of potential difference when subjected to temperature difference. Thermoelectric materials are associated with the concept of high electrical conductivity like crystals and low thermal conductivity to that of glass. Nanothermoelectric materials can decrease further the thermal conductivity through phonon scattering. Electrical characterization suggests the presence of both NTCR and PTCR behavior in the sample, and hence, it explores the application in thermistor/resistance temperature detector's (RTD) and low dielectric constant and loss to electro-optical and higher conversion efficiency to storage devices. Additionally, impedance spectroscopy helps in the study of electrochemical systems and solid-state devices wherein the transition of metal-insulator is an add-on to the research.

1. Introduction

Strongly correlated electron systems consisting of insulators and electronic materials show uncommon, productive properties including colossal magnetoresistance, electromagnetic, spin-charge partition, transitions into metal-insulator, half-metallicity, and heavy fermion behavior and superconductivity. Cobalt in the transition metal oxides A$_{n+2}$Co$_{n+1}$O$_{2n+2}$ (A = Ca, Ba, Sr) adopt different oxidation states and probes its entry into electrochemistry and medical diagnostics. The overture studies of the BaCoO$_{3-\delta}$ system on powder samples revealed numerous hexagonal polytypes [1] that have not

been discretely distinguished, accredited to BaCoO$_{3-\delta}$ (15H 3-δ <2.23, 12H (2.43<3-δ <2.49), 7H (2.52<3-δ <2.575), 2H-2.85<3-δ <3.0), and orthorhombic BaCoO$_{2.07}$ and BaCoO$_2$, while orthorhombic BaCoO$_{2.63}$ formed after annealing in O$_2$ had two other phases assigned to the cubic BaCoO$_{2.72}$ with a co-precipitate product non-indexed phase BaCoO$_{2.31}$ [2]. The specimen prepared by the sol-gel method is a low-temperature process involving the precursor solution inclusive of metal salts, a chelating agent (citric acid), and a diol (ethylene glycol). The advantages of the method are chemical composition with varied parameters of temperature, time, and atmosphere and are controllable to synchro-
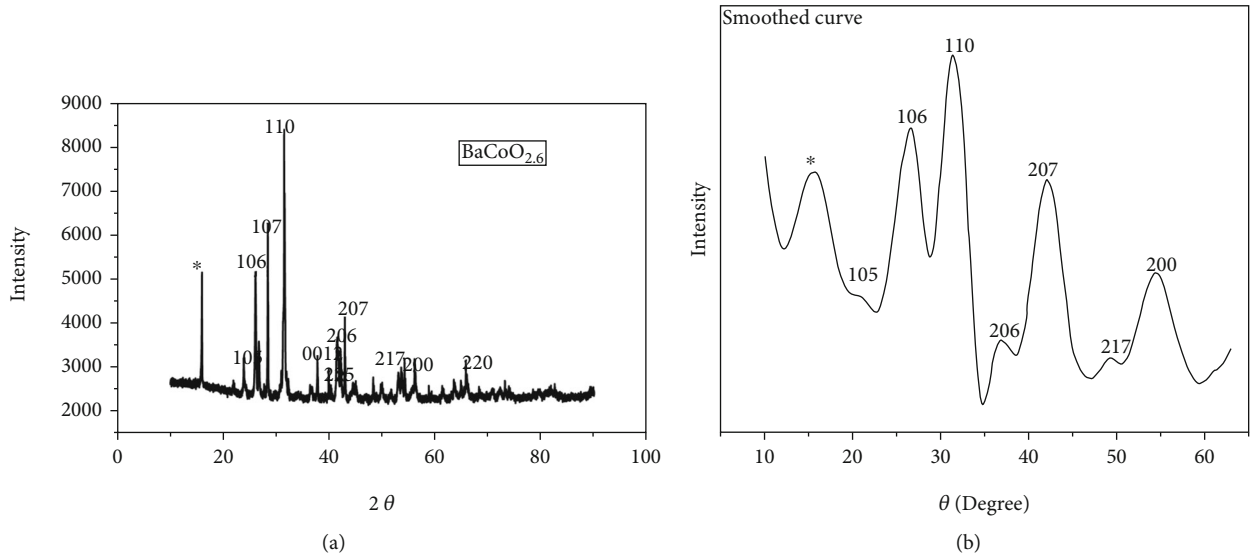
FIGURE 1: (a) Powder X-ray diffraction pattern (XRD) of the sample $BaCoO_{2.6}$ prepared by conventional sintering. (b) Main peaks of Figure 1(a) are highlighted.
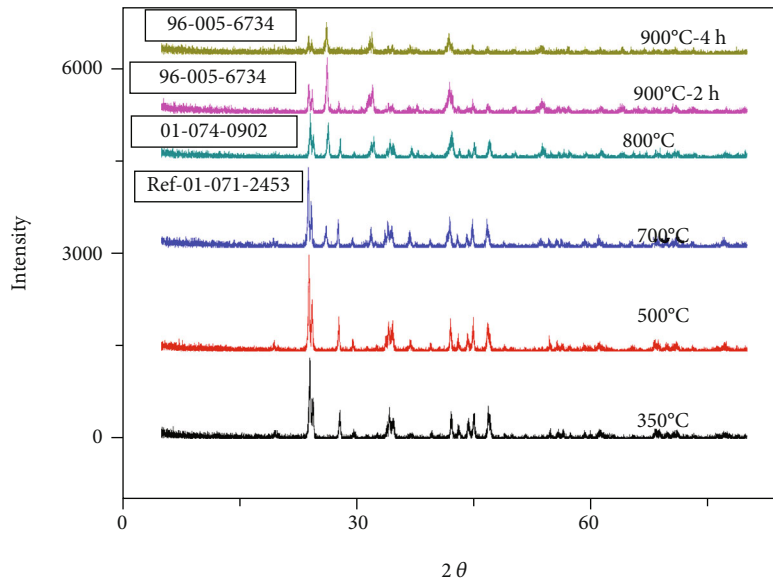

FIGURE 2: The multiphase transitions of the resultant product over an extrinsic temperature range.

nize with the structural and morphological characteristics of the specimen. Eventhough there are disadvantages like sensitive to moisture and time-consuming process with several steps, the advantages such as low-cost, flexible synthetic route, easy to implement overshadows.

Though several methods have been adopted for the synthesis of $BaCoO_{3-\delta}$ using $BaNO_3$ and $CoNO_3$ (600°C-12 h, 900°C-10 h) and $BaCO_3$, Co_3O_4 precursors (≈1200 K-2 days) [3–6], this is the first study to synthesize nano powder $BaCoO_{2.6}$ using the sol-gel method with lesser annealing time and analyze its physicochemical properties that include Seebeck coefficient, ac and dc conductivity studies, dielectric properties, PTCR/NTCR behavior, and the metal-insulator transition.

2. Materials and Methods

2.1. Experimental Details. The nanocrystalline sample has been prepared by a citrate-nitrate gel method using varying compositions of starting materials, such as Ba $(NO_3)_2$, Co $(NO_3).6H_2O$, citric acid, and ethylene glycol, which were taken in a stoichiometric ratio of $Ba_3Co_4O_9$, dissolved in deionized water with pH 2 at 309 K, and placed on a hot plate with a magnetic stirrer at 80°C for 2 hours to form the gel, which was then transferred to a platinum crucible and kept in an electric furnace and heated at 700°C for 5 hours. At 310°C, auto-combustion lasting for a few seconds occurred [7, 8], and the ash product was manually ground and then pressed into pellets at 1 Gpa, sintered for 120
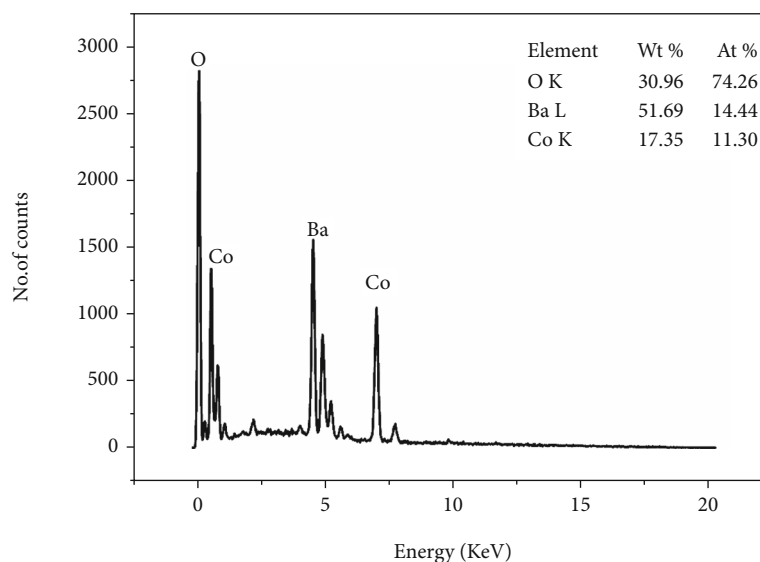
FIGURE 3: The elemental analysis (EDAX, 1 KeV to 20 KeV) of the synthesized sample.
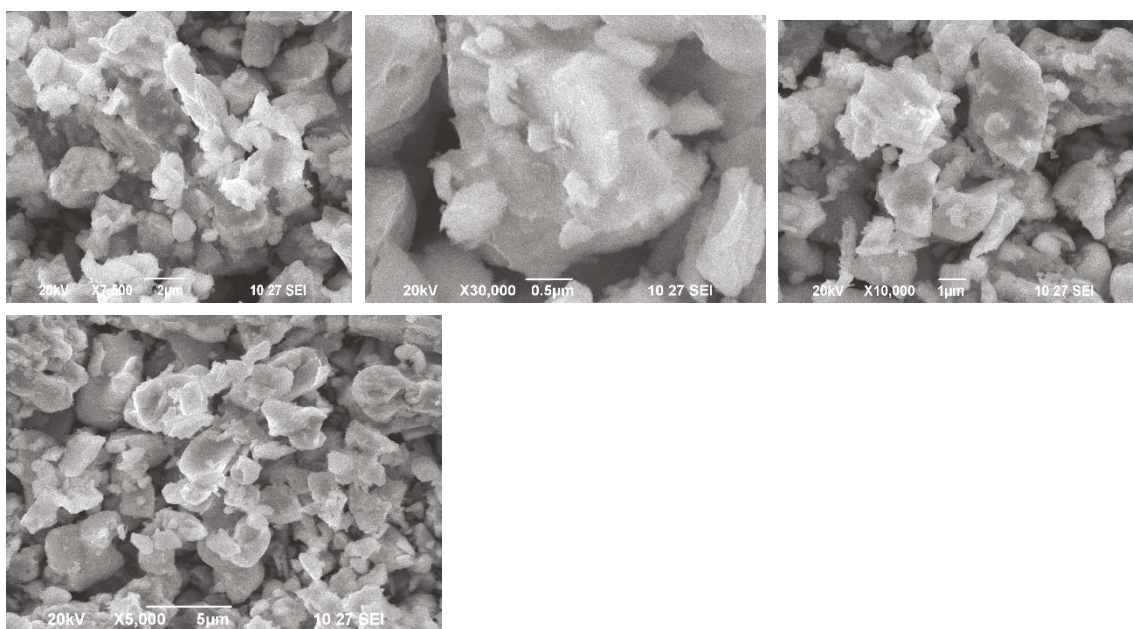

FIGURE 4: SEM image with different magnifications of $BaCoO_{2.6}$.

minutes at 900°C in the atmosphere, and left in the furnace for natural cooling [9] (precaution: due to the release of nitrogen oxides, heating has to be done in a closed chamber with adequate care).

2.2. Analysis of the Structure

2.2.1. X-Ray Diffraction (XRD) Method. The prepared sample was characterized by XRD with a Bruker-axs D8 diffractometer (40 KV, 30 mA) and DIFFRAC software, Bragg-Brentano reflection geometry, and treatment with $CuK\alpha$ (=1.05418 A). The data was collected between 10°C and 90°C in steps of 0.005 and at a scanning rate of 1/minute.

The microstructural features and composition were studied using a scanning electron microscope (JOELJSM6390, Japan) having (EDAX) capability.

2.3. FTIR Analysis of the Synthesized Nanomaterial. Infrared spectra (FT-IR) from the sample were observed in the 400-4000 cm^{-1} via Fourier transform-infrared spectrometer (Perkin-Elmer spectrum).

2.4. Electrical Transport Measurements. Shaped rectangular bars of 12 mm ∗ 4 mm ∗ 4 mm of the sample was used for the recording of Seebeck coefficient (S) and electrical resistance simultaneously (Seebsys, NorECS AS Norwegian
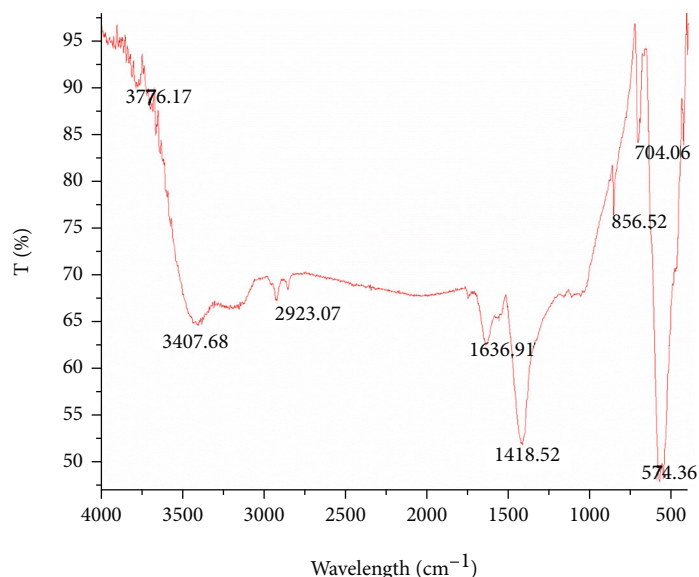
FIGURE 5: FTIR spectrum of synthesized nanomaterial $BaCoO_{2.6}$.

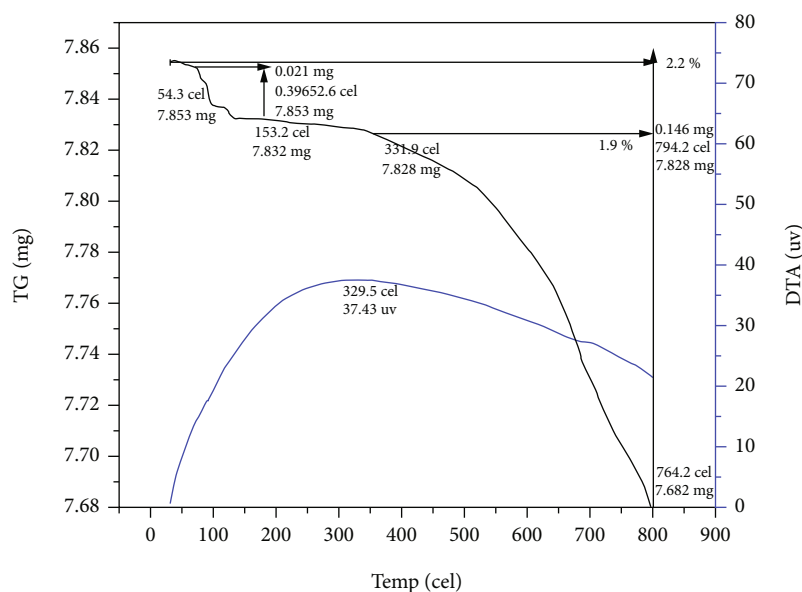FIGURE 6: TG/DTA curve synthesized nanomaterial $BaCoO_{2.6}$.

Electro Ceramics) for the temperature of 30°C to 600°C in atmospheric air for a standard 4-probe technique with wide frequency range to evaluate dielectric constant as well as ac conductivity (Waynker multicomponent precision analyzer 6440B).

3. Result and Discussion

3.1. Structural Analysis

3.1.1. XRD of the $BaCoO_{2.6}$ Nanoparticle. Figure 1 displays the powder XRD of the $Ba_3Co_4O_9$ nanoparticle prepared by conventional sintering. The different crystalline phases

present in the sample were confirmed by comparing the XRD pattern to reference phases of the Xpert high score plus software. Major peaks had been associated with the $BaCoO_{2.6}$, specified by its reflection planes (Figure 1), in concurrence with the preceding reports JCPDS01-071-2453) [6]. The compound $BaCoO_{2.6}$ becomes crystalline in the space group P63/m m c symmetry in the lattice parameter, $a = b = 5.6710A^0$ and $c = 28.5450A^0$, and the unit cell volume $(V) = 795.024A^3$. With the XRD data, the evaluation of the size of the crystallite was carried out by Scherrer equation, $D = k\lambda/\beta Cos\theta$, where D is the crystallite size (nm); β is the full width at half maximum of the diffraction peak; k is the shape factor (0.9); λ is the X-ray wavelength, and θ is
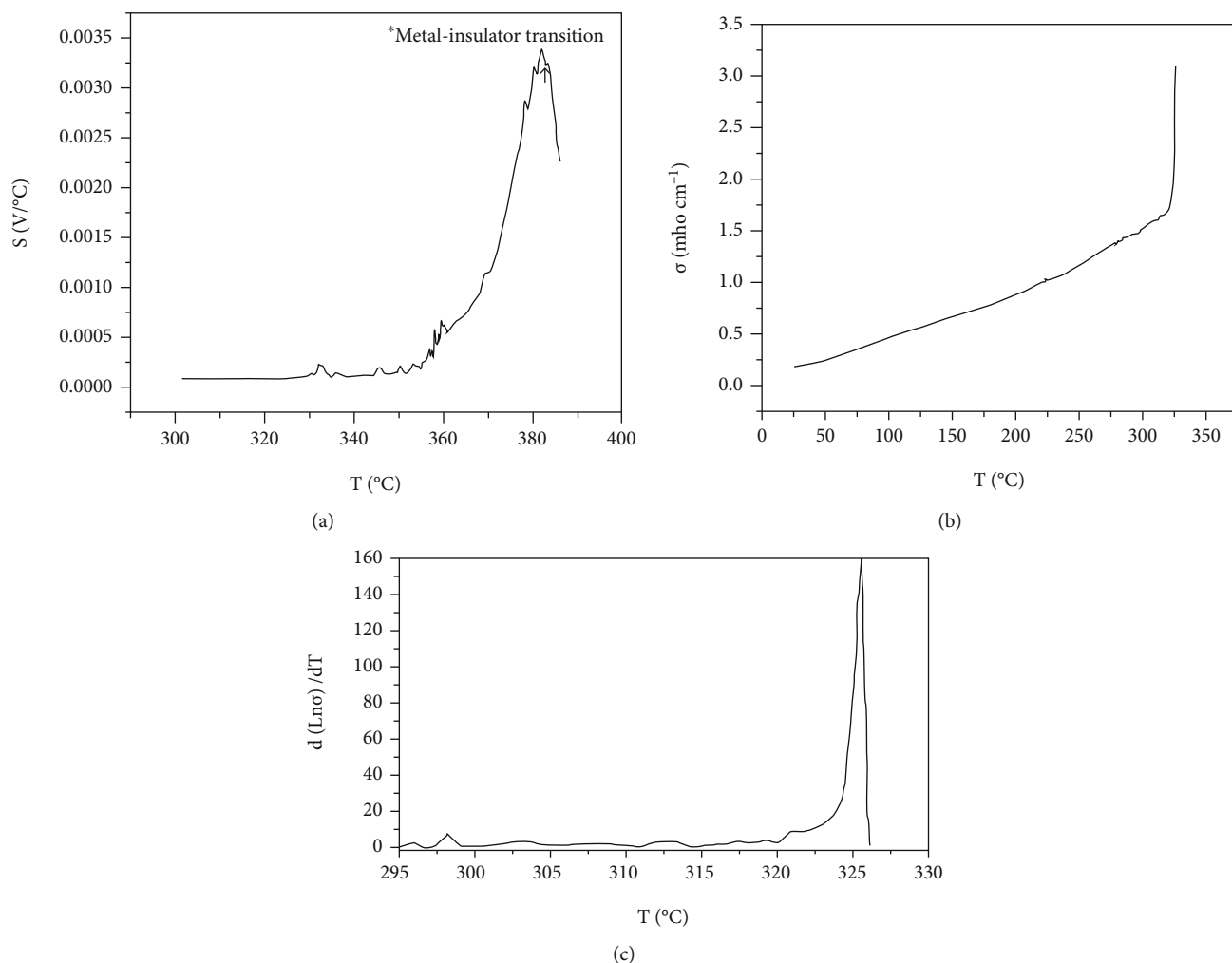
Figure 7: (a) The Seebeck coefficient (S). (b) Electrical conductivity. (c) $(\partial W) = \partial ln\sigma/ln T$. of synthesized nanomaterial $BaCoO_{2.6}$.

the diffracting angle. The average crystallite size of the most intense peak (110) plane of $BaCoO_{2.6}$ was assessed and found to be approximately 25.26 nm. The crystallite size corresponds to the coherently diffracting domain size and not to the particle size. The peak with an asterisk (∗) may correspond to $Ba_3Co_4O_9$ or $BaCo_2O_4$ (JCPDS23-110) secondary phase [8–10].

The multiphase transitions of the $BaCoO_{2.6}$, over an extrinsic temperature range are shown in Figure 2. A selective list of efficient compounds certified as crystal structures is only specified completely in recent studies ($BaCoO_{2.6} \rightarrow BaCoO_3 \rightarrow Ba_3Co_2O_6 (CO_3)_{0.6}$) from 973 K to 1173 K and is the successive phase transition sequence. Not much detectable phase of barium cobaltite was found in annealing temperatures of 623 K and 773 K. Comparing the plot's e and f, we find that the diffraction peak of (e) is higher than the diffraction peak of (f), indicating that crystallization of (e) to be more than the crystallization of (f) [3, 11]. Hence, the start-up temperature for the synthesis of $Ba_3Co_2O_6$ $(CO_3)_{0.6}$ may be assumed to be 900°C for 2 h. The different characteristic properties of $BaCoO_3$ and $Ba_3Co_2O_6 (CO_3)_{0.6}$ will be analyzed in our future work.

3.2. Elemental Analysis of the Sample. The elemental analysis (EDAX, 1 KeV to 20 KeV) of the synthesized sample in Figure 3 shows the presence of expected elements. Figure 4 represents the SEM image with different magnification and the images reveal the grains in the range of 0.5 μm-5 μm.

3.3. FTIR Analysis of the Sample. FT-IR analysis was carried out for detecting the presence of the functional groups and for analyzing the reaction mechanisms during the sol-gel process (Figure 5). The band specific to the NO_3^- is found at 1419.62 cm^{-1}, and the peak around 842 cm^{-1} is associated with the distortion vibration of N-H bending mode. The absorption peak situated below 836 cm^{-1} is due to barium-cobalt-oxygen stretching vibrations [12, 13]. The slight shoulder around 1636.51 cm^{-1} denotes the asymmetrical stretched vibration of carboxylate anion and carbonyl groups [14]. The OH- group at 3407.68 cm^{-1} and 2923.07 cm^{-1} owes to the absorbed water during the sample preparation [15].

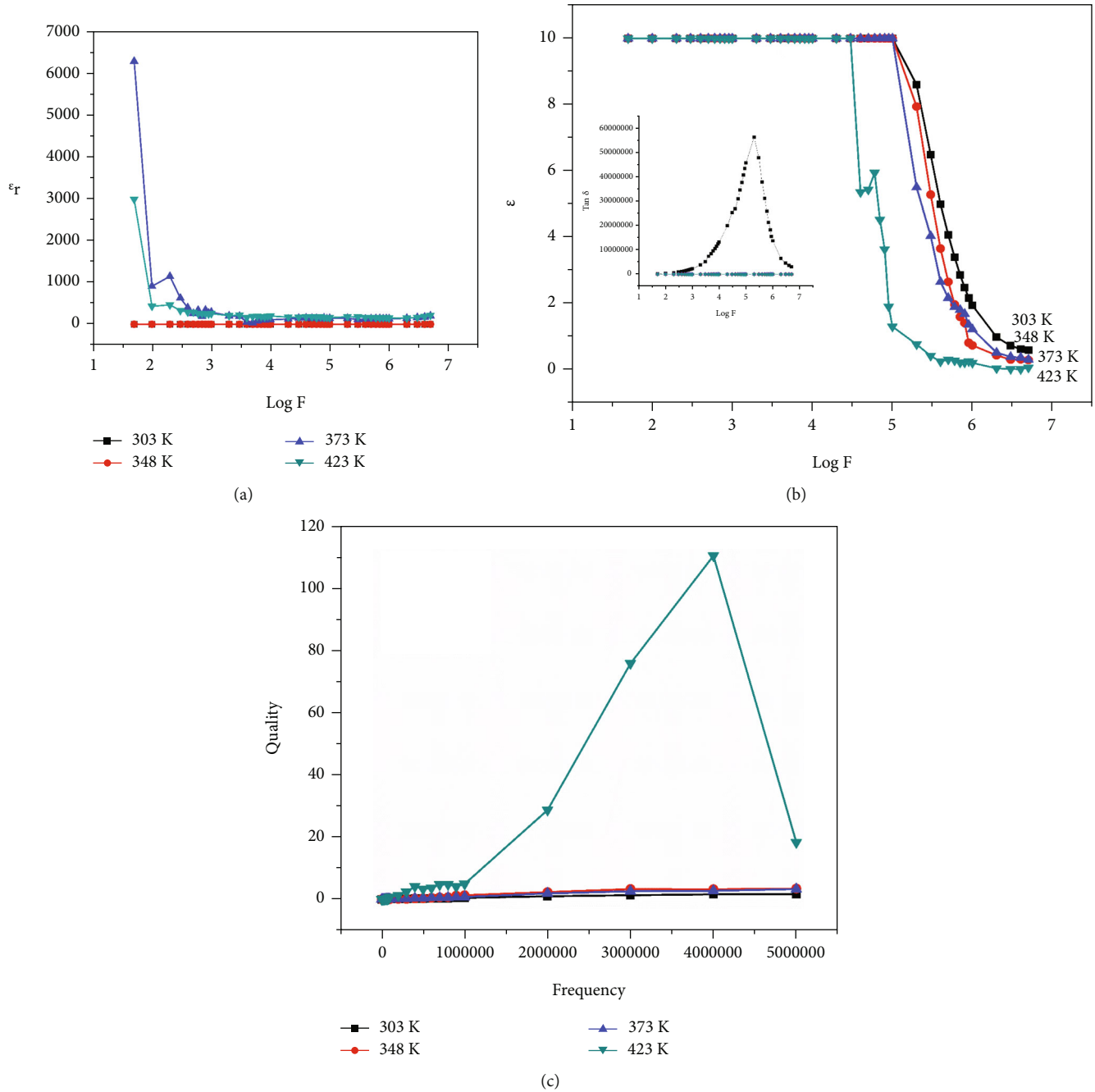*3.4. Thermal Properties.* The TGA/DTA spectrum for $BaCoO_{2.6}$ is illustrated in the Figure 6. The reduction in

(a)

(b)

(c)

FIGURE 8: (a) Dielectric constant (ε'). (b) Dielectric loss and inset: loss factor (($\tan \delta = \varepsilon''/\varepsilon'$)). (c) Quality concerning variation in the frequency of synthesized nanomaterial $BaCoO_{2.6}$.

weight ($\approx 0.3\%$) at T <150 C is mainly due to the loss of constituents such as water, solvents with low molecular weight, or gas desorption between 150°C and 250°C ($\approx 1.9\%$), additives, or crystallization and first decomposition products. The total weight loss accounts for $\approx 2.2\%$ at 300°C, and henceforth, no weight loss occurs indicating the completion of the combustion process and the formation of oxide phases.

3.5. Transport Properties. The Seebeck coefficient (S) is the ratio of the magnitude of the induced voltage to the temper-

ature gradient across a material. It is caused by charge carriers diffusion and phonon drag. The (S) is very low for metals and much larger for semiconductors. The value of S determined in the present study increases with temperature ($\approx 40 \mu$V/C) indicating a metallic phase from 35°C to 150°C, thereafter decreasing with increasing temperature in the insulating phase as shown in Figure 7(a). The rise and fall in the magnitude of (S) with temperature increase imply the predominance of both thermally accessible transport states and the carrier density [12–14]. To further characterize the temperature-dependent conductivity, the graph was
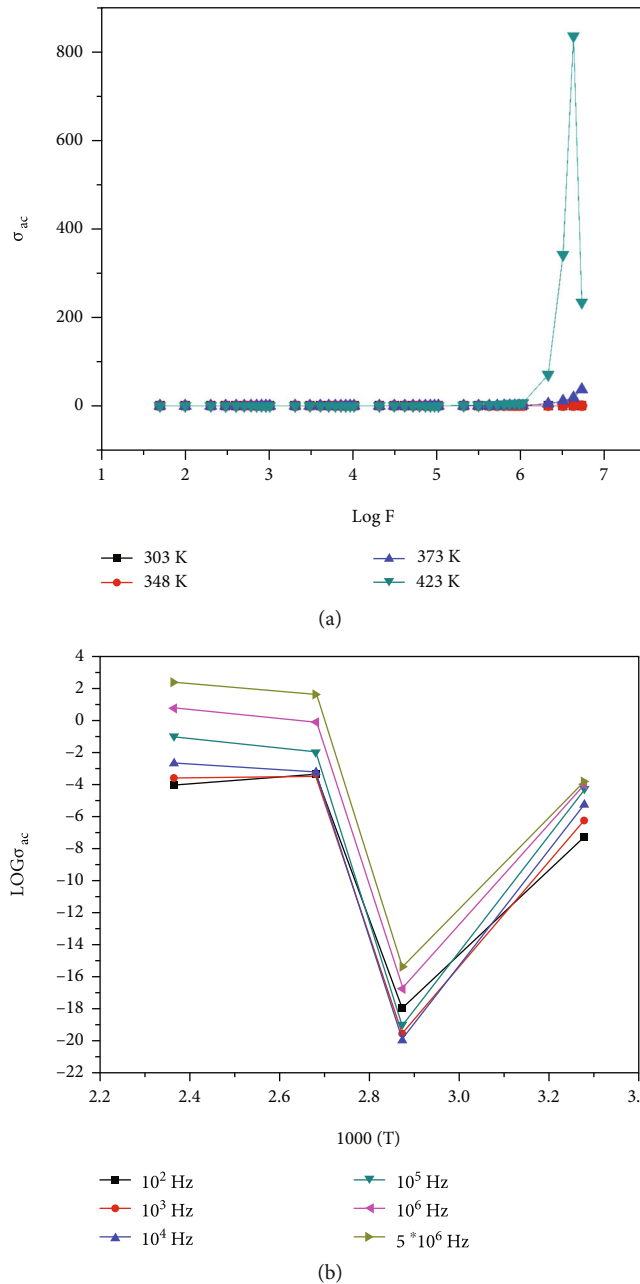
(a)

(b)

FIGURE 9: (a and b) Variation of ac conductivity concerning frequency and temperature.

plotted against the charge carrier transport properties, the reduction in activation energy, $W((\partial W) = \partial ln\sigma/lnT.)$, and temperature. The slope of W exemplifies the conduction mechanism as per Mott's metal-to-insulator transition (MIT) model for disordered semiconductors (Figure 7(c)). The raise in electrical conductivity (positive slope) with an increase in temperature up to 325°C and thereafter decline (negative slope) with an increase in temperature may be attributed to PTCR/NTCR behavior, respectively, wherein the PTCR's usage in current overload protection devices [15–17]. Figure 7(b) shows a transition at 325°C in conductivity of the sample, and this may be due to the casting back of charge carriers in the material. Transport properties like

TABLE 1: Activation energy of the sample.

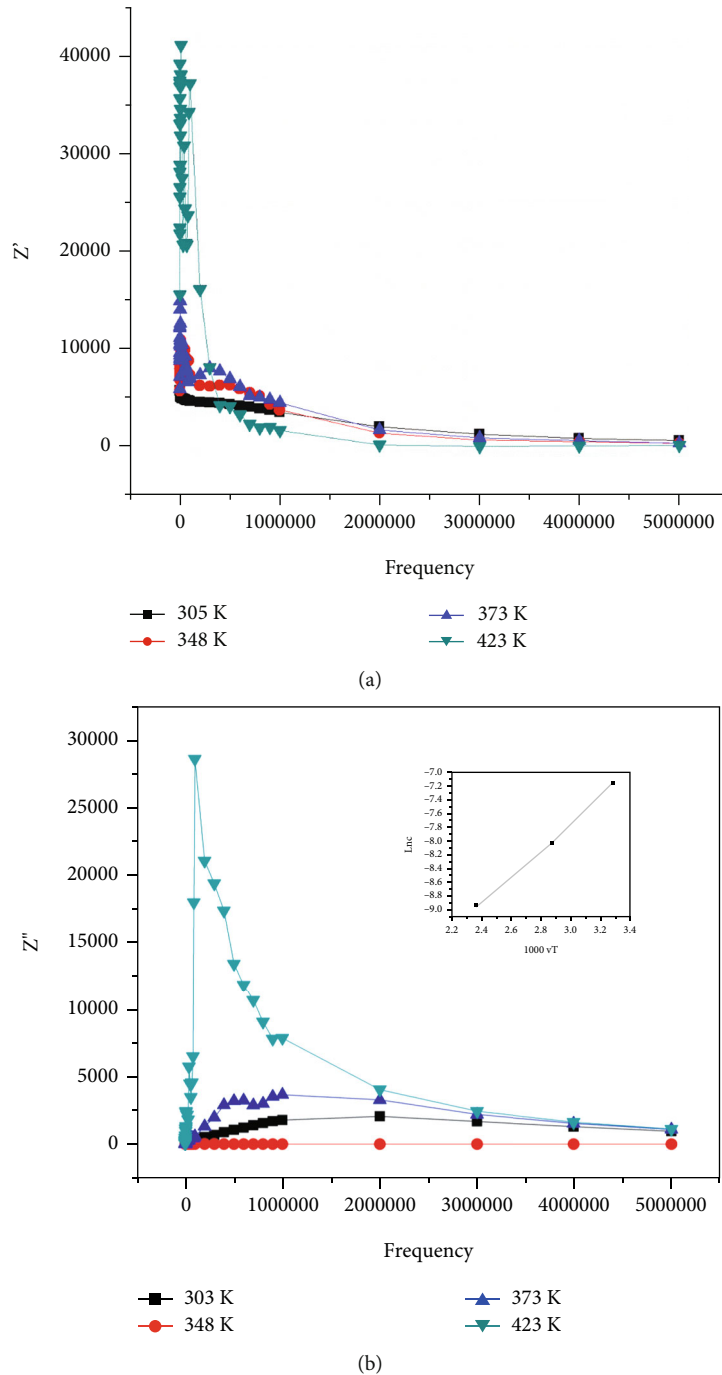| Frequency (Hz)	Activation energy E_a (eV) Temperature range	
	Region I	Region II
10^2	1.35	1.16
10^3	1.38	1.09
10^4	0.91	1.24
10^5	1.27	1.14
10^6	1.10	0.97
$5 * 10^6$	1.09	0.83

(a)

(b)

FIGURE 10: (a and b) Z' and Z'' variation with frequency and inset: relaxation time.

electrical conductivity and Seebeck coefficient may be enhanced through doping, and by increasing the density of the sample, the density of the sample remains 74% theoretical density [18].

3.6. Dielectric Properties. The enriched knowledge about dielectric analysis may shed light on the electrical properties of a material medium with varied temperatures and frequency. Dielectric constant (ε') shown in Figure 8(a) initially decreases abruptly with the rise in frequency and is stable at

higher frequency assuring that at the further side of a specific frequency of applied electric field, the exchange of electrons does not follow the alternating field. Therefore, polarization reduces resulting in a reduction in the dielectric constant (ε') [19]. From Figure 8(b), it is observed that the constant low-frequency dielectric loss may be due to the blocking of charge carriers at the cathode resulting in the formation of space charge polarization, and the abrupt decrease at 100 kHz may be the sign of thermal activation and hopping of charge carriers on a lattice surface.
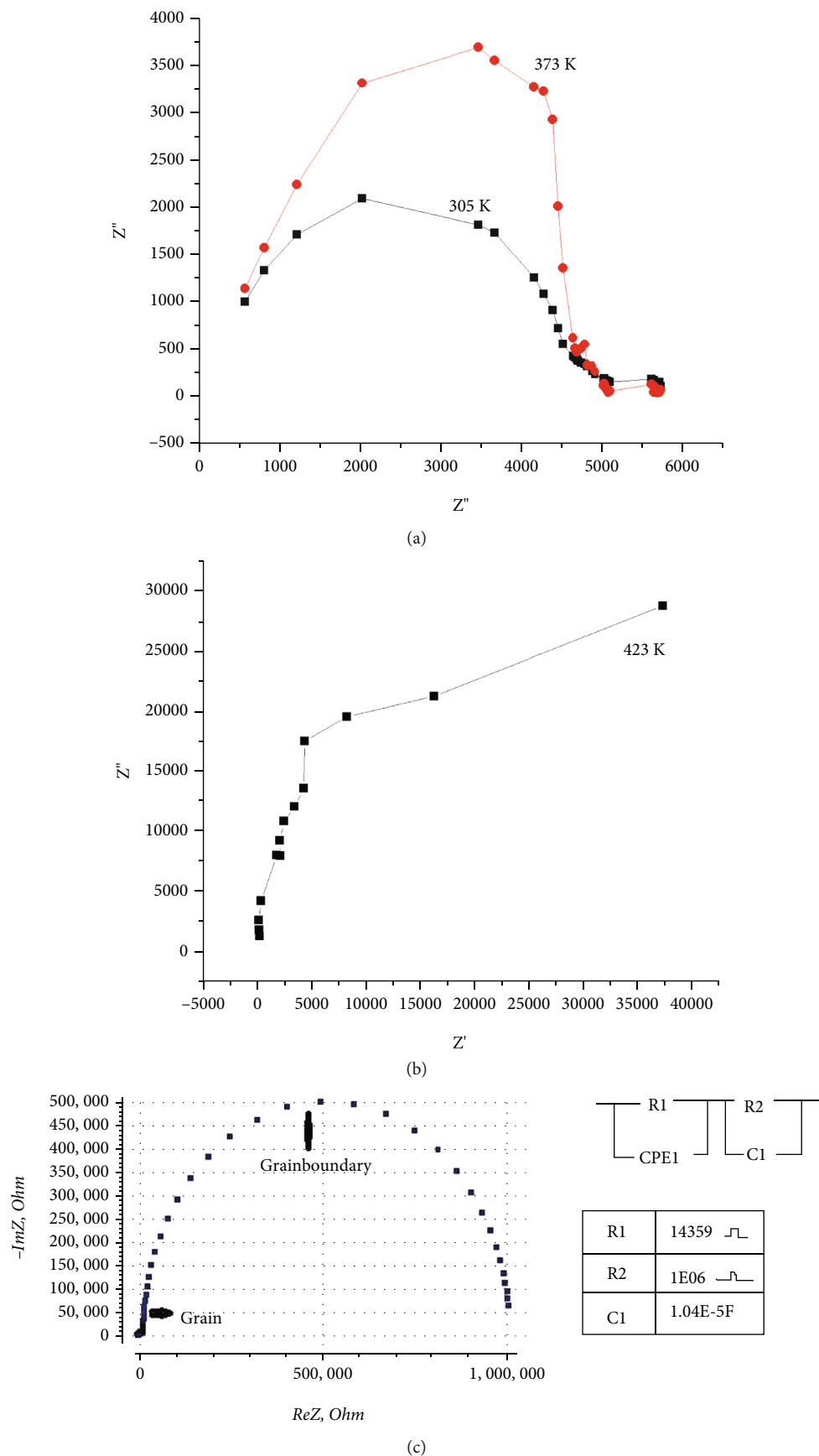
(a)

(b)

(c)

FIGURE 11: (a–c) Nyquist plot at room temperature, 373 K and 423 K, and equivalent circuit of synthesized nanomaterial $BaCoO_{2.6}$.
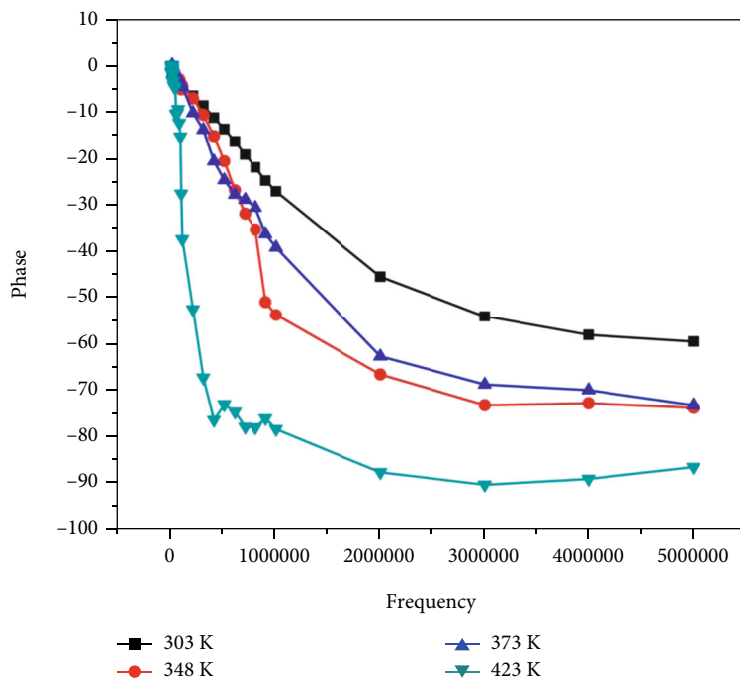
FIGURE 12: Variation of phase with frequency.

Figure 8(b)-inset shows the loss tangent (tan $\delta = \varepsilon''/\varepsilon'$) curve wherein the resonating hopping frequency of electrons to the frequency of the applied electric field marks the peak indicating maximum electric energy being transmitted to the electrons and shooting up of loss at resonance [20]. Thus, the sample is more of energy storage with an extended lifetime and reduced charge-discharge time and less energy dissipater (Figure 8(c)) with applied frequency and temperature indicating high conversion efficiency [21, 22].

3.7. Ac Conductivity Studies. Figure 9(a) of ac conductivity figures the NTCR (negative coefficient of the temperature) behavior of the synthesized nanoproduct.

Figure 9(b) denotes calculations of (σ_{ac}) and (E_a) ac conductivity and activation energy, respectively, of the sample using the relation $\sigma = \omega \varepsilon' \varepsilon_0 tan\delta$ and $\sigma = \sigma_0 \exp (-E_a/k_B T)$, where ε_0 is the vacuum permittivity, k_B is the Boltzmann constant, $\omega = 2\pi f$ is the angular frequency, and σ_0 is the preexponential factor [23]. For most dielectric ceramics, conduction has a high value and also remains constant for all frequencies at higher temperatures (region III). In the region I, the ac conductivity (σ_{ac}) does not follow the conductivity relation and is considered a metallic behavior, also observed in the Seebeck measurement (Figure 7(a)). In the region II (mid-temperature region), the conductivity differs exponentially with the temperature that is no longer linear wherein the change in slope (from positive to negative) may be attributed to the facts such as a mixed type of conduction inducted by thermally activated charge carriers and the oxygen vacancies in the nanoproduct [24–27]. The presence of oxygen vacancies and transfer of charge carriers concerning metal-insulator connects the sample probe into the analysis of critical temperature of high-temperature superconducting cuprates, usage as catalysts for hydrogen evolution reaction in support of green energy, as

the secondary power supply in integrated circuits, and current overload protection devices [28–30].

3.8. The Activation Energy of the Synthesized Nanomaterial. The activation energy (E_a) of the product evaluated from the slope of log σ_{ac} vs 1/T curve is listed in Table 1. It is clear that the lower mobility (i.e., low conductivity) with higher activation energies corresponds to the ionic conduction in region I. On the other hand, electronic conduction in the region II is connected to relatively highest mobility (i.e., high conductivity) as well as the lowest activation energy [31, 32]. The E_a value in the region I and region II of the sample varies from 0.9 eV to 1.3 eV and 0.8 eV to 1.2 eV, respectively.

3.9. Impedance Analysis. This technique aids in separating the imaginary and real components of the complex impedance quantities to comprehend the structural property relationship of the sample. Figure 10(a) exhibits the difference in the real part of impedance (Z') as a function of frequency at various temperatures. The data indicate a decrease in (Z') in the low-frequency region followed by saturation in the high-frequency region (>100 kHz). The values of Z' merging at higher frequencies suggest the discharge of space charge carriers [24]. The differences in the imaginary part of impedance (Z'') with frequency (i.e., loss spectrum) at various temperatures in Figure 10(b) reveal that peaks are found at temperatures >100°C. The distinct shift among peaks with a magnitude increase of Z'' for temperature suggests the contribution of immobile electrons. The position of the Z'' peaks shifting to the lower frequency on enhancing temperature and moderation in a peak width indicates the chances of the relaxation times distributed and the series capacitance presence [33, 34]. The occurrence of more polarization
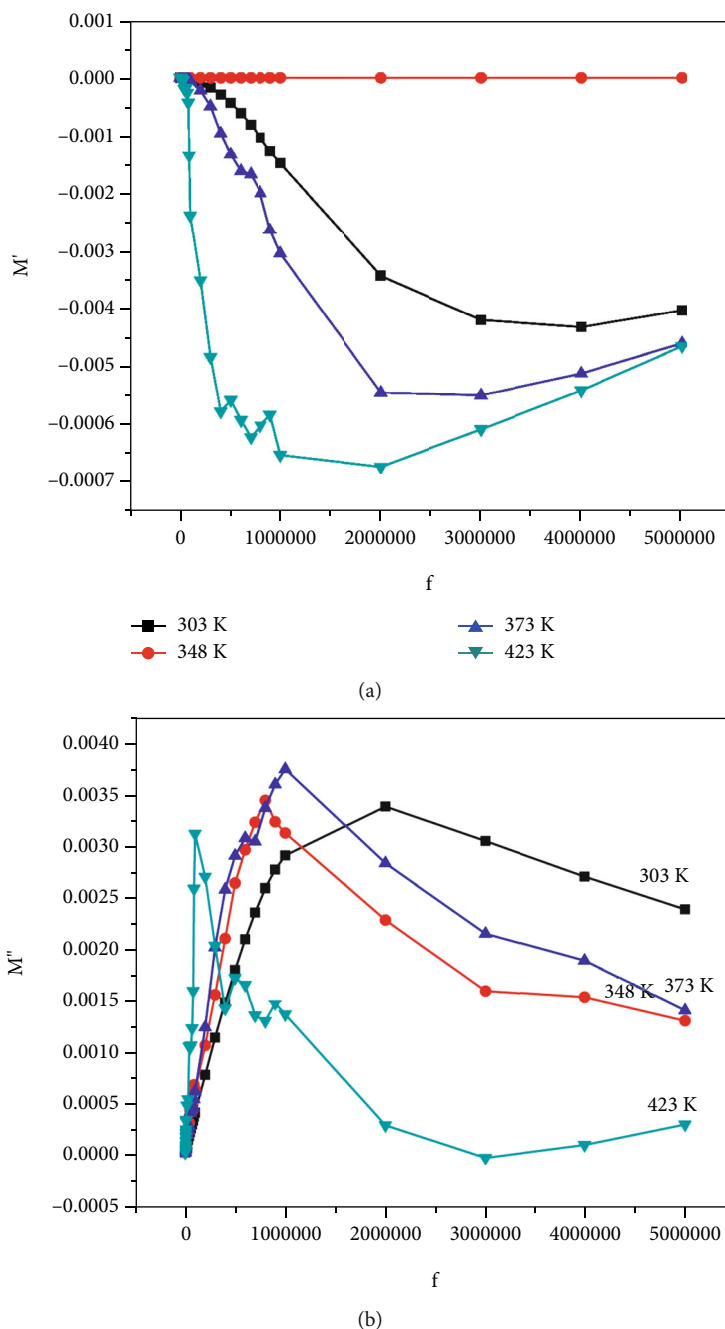
(a)

(b)

Figure 13: (a and b) Variation of M' and M'' with the frequency of the synthesized nanomaterial BaCoO$_{2.6}$.

charge transfer processes can be inferred in the impedance plot through the presence of greater than one arc [26]. The frequency consistent with the maximum of Z'' correlates with the relaxation time with the expression: $\zeta \omega_{max} = 1$, where ω is the angular frequency [29]. Hence, the relaxation effect, as well as asymmetric peak broadening, is indicative of the non-Debye type of relaxation.

Figure 10(b)-inset indicates the difference of relaxation time (inferred from loss spectrum) with an inverse of absolute temperature ($10^3/T$) following the Arrhenius law given by $\zeta = \zeta_0 \exp (E_a/k_B T)$, where K_B is the Boltzmann constant, ζ_0 is the preexponential factor, and E_a is the activation energy. The typical data confirms a temperature-dependent relaxation process with the distribution of relaxation time in 10^{-6} to 10^{-4} sec indicating an escalation in the process dynamics (i.e., charge/carrier transport) in the material due to elevation in temperature [35].

3.10. Nyquist Plot at Different Temperature. Nyquist plot points out the overall contribution percentage of bulk or grain boundary components which is accredited to the quality and electrical homogeneity of the material as for the bonding between the sintering/microstructure to the AC response. The plot also contributes to the magnitudes of the component
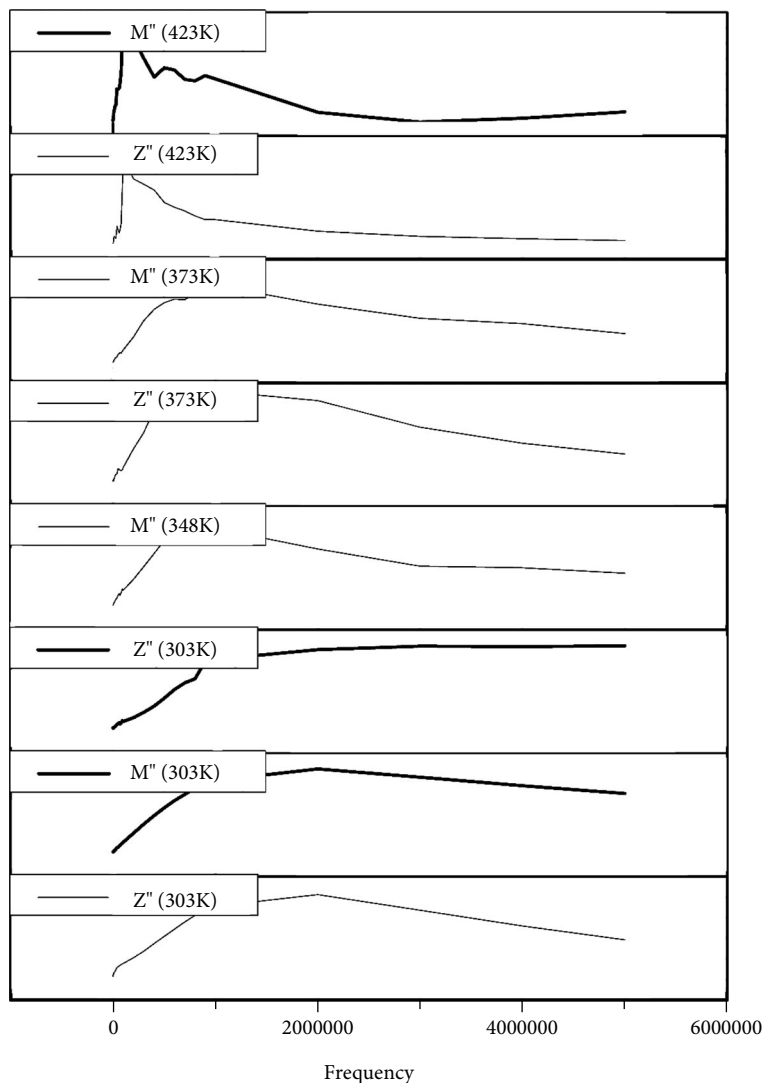
FIGURE 14: Combined plot of $Z^{''}$ and $M^{''}$ of synthesized nanomaterial $BaCoO_{2.6}$.

resistances and capacitances and picturization of redox reactions occurring at the electrode cells [36]. Nyquist plot ($Z^{'}$ vs. $Z^{''}$) at room temperature, 373 K and 423 K, with corresponding equivalent circuit is best fit obtained using electrochemical impedance analyzer (EIS) software (for 100 C as shown in Figures 11(a)–11(c) with the possibility of two semicircles, highlighting the presence of grain boundaries and grains within the sample. The observed increase in the size of semicircular arcs with an increase in temperatures is related to the increase of capacitance, indicating dielectric (capacitive) behavior of the sample (resulting in phase -90°C, Figure 12) in the sample [37]. As the size (height) of the semicircles observed in the impedance plot depends on the resistive responses of the components in the sample, it is hard to acknowledge the responses emerging from the grain and grain boundary relating to their high capacitance values [24, 38, 39].

3.11. Modulus Studies. To identify the nature of relaxation behavior and to distinguish long-range conduction from short-range hopping motion, frequency dependence on the imaginary part of electric modulus is observed (Figure 13(a)). The M value is low in the range of low frequency. Moreover, dispersion is seen with an increase in the frequency that can be corroborated by an insufficient restoring force regulating the movement of the charge carriers influenced by an induced electric field. The result affirms the exclusion of the electrode effect in the test sample [24]. In the plot of $M^{''}$ (f) shown in Figure 13(b), the peaks shift to a lower frequency side with the elevation in temperature, and the bit sharper peak exists at a low frequency (~460 Hz) at the highest temperature (150°C) indicating that the ions can travel over long distances, i.e., charge carriers can carry out hopping well between the sites. The high-frequency peaks corresponding to lower temperatures suggest the confinement of ions within their wells with localized motion. This behavior shows that the dielectric relaxation is an unusual thermally activated type wherein the hopping mechanism of charge carriers dominated intrinsically [38].

The power of synergistic use of both impedance and modulus spectroscopy $Z^{''}$ vs. $Z^{'}$ plot emphasizes the phenomenon of largest resistance. Contrastingly, $M^{''}$ vs $M^{'}$
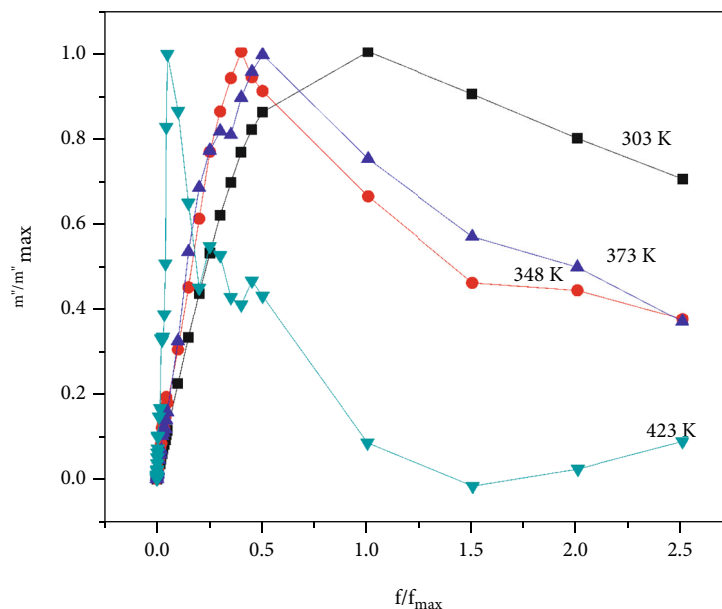
FIGURE 15: M''/M''_{max} vs f/f_{max} of synthesized nanomaterial $BaCoO_{2.6}$.

picks up those of the smallest capacitance highlighting that the relaxation process is a short- or long-range motion of charge carriers. The impedance peaks (Z'') correspond to R/2 and the modulus peak to that of $e_0/2C$ of that particular element [40]. Figure 14 shows the selective plot of impedance (Z''), modulus (M'') variation, and frequency due to different temperatures. The highest values coincide at a specific frequency in the synthesized $BaCoO_{2.6}$ indicating a similar time gap of impedance as well as modulus spectra, and also the matching of peaks at all temperatures suggests the long-range movement of charge carriers [41, 42]. Additionally, in the short-range peaks, Z' and M' are observed in diverse frequencies, and long-range transmission of charge carrier peaks is seen at the same cycles.

The validation of the distribution of relaxation times with temperature dependence was done by plotting the M'' in weighted coordinates, i.e., M''/M''_{max} vs f/f_{max} (f_{max}-loss peak frequency) (Figure 15). A perfect overlapping of curve bands in a single master curve was not observed. The result conveys the conduction mechanism being altered with temperature exhibiting non-Debye type behavior and mixed conduction at high temperatures [39, 43].

4. Conclusion

The synthesized $BaCoO_{2.6}$ powder using the sol-gel method was characterized by different techniques. The Seebeck coefficient (S) is positive, indicating p-type behavior and the graph confirms the metal-insulator transition in the material. The FTIR study confirmed the presence of functional groups, and the positive value of the Seebeck coefficient (S) indicates p-type behavior. The electrical studies suggest both NTCR and PTCR behavior in the sample and its applications in thermistor/RTD. The characteristics of low dielectric constant, dielectric loss, and low dissipation factor with

high frequency indicate enhanced optical quality and higher conversion efficiency, hence the sample's research in electro-optical and storage devices with less charge-discharge time. The characteristic reduction in low dielectric constant and high-frequency dielectric loss concludes the enhanced optical quality and low dissipation factor to energy storage/capacitors, and the features of MI transition suggest the sample probe into electrical and optical switching devices and secondary power supply in integrated devices. The electrical studies suggest both NTCR and PTCR behavior in the sample and its applications in thermistor/RTDs. The impedance studies of the sample affirm the existence of grain in bulk as well as the grain boundary effects. The complex impedance spectroscopy study suggests the long-term mobility of charge carriers as well as non-Debye type with mixed conduction in the material. More studies are required to shower an insight into deducing further information and discern for a better interpretation of the results obtained.

Data Availability

All data generated or analyzed during this study are included in the published article.

Conflicts of Interest

There exists no conflict of interests.

References

[1] M. Zanne and C. Gleitzer, "Bafeo$_3$-X Polytype," *Bulletin de la Societe Chimique de France*, vol. 5, p. 1567, 1971.

[2] O. Mentré, M. Iorgulescu, M. Huvé et al., "BaCoO$_{2.22}$: the most oxygen- deficient certified cubic perovskite," *Dalton Trans*, vol. 44, no. 23, pp. 10728–10737, 2015.

[3] J.-J. Choi, W. Qin, M. Liu, and M. Liu, "Preparation and characterization of (La$_{0.8}$Sr$_{0.2}$)$_{0.95}$MnO$_{3-\delta}$(LSM) thin films and LSM/LSCF interface for solid oxide fuel cells," *Journal of the American Ceramic Society*, vol. 94, no. 10, pp. 3340–3345, 2011.

[4] P. M. Botta, V. Pardo, D. Baldomir, C. de La Calle, J. A. Alonso, and J. Rivas, "Dynamic magnetic behavior of BaCoO$_3$ quasi-one-dimensional perovskite," *Physical Review B*, vol. 74, no. 21, article 214415, 2006.

[5] K. Iwasaki, T. Yamamoto, H. Yamane et al., "Thermoelectric properties of Ba$_3$Co$_2$O$_6$(CO$_3$)$_{0.9}$ containing one-dimensional CoO$_6$ octahedral columns," *Journal of Applied Physics*, vol. 106, no. 3, article 034905, 2009.

[6] A. J. Jacobson and J. I. Hutchison, "The structure of BaCoO$_{2.6}$ by a combination of high-resolution electron microscopy and neutron powder diffraction," *Journal of the Chemical Society, Chemical Communications*, vol. 3, pp. 116-117, 1976.

[7] C. Callea, J. A. Alonso, and M. T. Fernández-Díaz, "Polymorphism of Ba$_{1-x}$Sr$_x$CoO$_{3-\delta}$ (0≤ x≤1) Perovskites: a thermal and structural study by neutron diffraction," *Verlag der Zeitschriftfu¨r Naturforschung*, vol. 63, no. 6, pp. 647–654, 2008.

[8] P. Carvillo, Y. Chen, C. Boyle, P. N. Barnes, and X. Song, "Thermoelectric performance enhancement of calcium cobaltite through barium grain boundary segregation," *Inorganic Chemistry*, vol. 54, no. 18, pp. 9027–9032, 2015.

[9] G. Constantinescu, S. Rasekh, M. A. Torres, M. A. Madre, A. Sotelo, and J. C. Diez, "Improvement of thermoelectric properties in Ca$_3$Co$_4$O$_9$ ceramics by Ba doping," *Journal of Materials Science: Materials in Electronics*, vol. 26, no. 6, pp. 3466–3473, 2015.

[10] J. Liu, X. Huang, D. Yang, G. Xu, and L. Chen, "Synthesis and physical properties of layered $_{BaxCoO2}$," *Dalton Transactions*, vol. 43, no. 41, pp. 15414–15418, 2014.

[11] M. Sopicka-Lizer, P. Smaczynski, and K. Kozlowska, "Preparation and characterization of calcium cobaltite for thermoelectric application," *Journal of the European Ceramic Society*, vol. 25, no. 12, pp. 1997–2001, 2005.

[12] C. Lamsel, *Electronic, thermoelectric and optical properties of vanadium oxides: VO$_2$, V$_2$O$_3$, and V$_2$O$_5$, [Ph.D. thesis]*, University of New Jersey, 2015.

[13] A. Chamoire, F. Gascoin, C. Estournes, T. Caillat, and J. C. Tedenac, "High-temperature transport properties of complex antimonides with anti-Th$_3$P$_4$structure," *Dalton Transactions*, vol. 39, no. 4, pp. 1118–1123, 2010.

[14] X. Huang and W. Zhang, "How does the spin-state of Co ions affect the insulator-metal transition in Bi$_2$A$_2$Co$_2$O$_8$ (A = Ca, Sr, Ba)," *Scientific Reports*, vol. 6, no. 1, pp. 1–9, 2016.

[15] X. Granados-García, X. Obradors, and J. B. Torrance, "Metallic state and the metal-insulator transition of NdNiO$_3$," *Physical Review B*, vol. 48, no. 16, pp. 11666–11672, 1993.

[16] M. Wang, C. Bi, L. Li et al., "Thermoelectric Seebeck effect in oxide-based resistive switching memory," *Nature Communications*, vol. 5, no. 1, p. 4598, 2014.

[17] D. Ruzmetov and S. Ramanathan, "Metal-insulator transition in thin film vanadium dioxide," in *Thin film metal-oxides: fundamentals and applications in electronics and energy*, Springer, Boston, MA, 2010.

[18] Z. E. Doktorgrades, *Anionic substitution in perovskite-type oxides, [Ph.D. thesis]*, Materials Science & Technology, Empa, CH-8600 Dübendorf, 2008.

[19] V. S. Shanthala, S. N. Shobha Devi, and M. V. Murugendrappa, "Ac conductivity and dielectric studies of polypyrrole copper zinc iron oxide nanocomposites," *IOSR Journal of Applied Physics*, vol. 8, no. 5, pp. 83–90, 2016.

[20] N. Singh, A. Agarwal, S. Sanghi, and S. Khasa, "Dielectric loss, conductivity relaxation process and magnetic properties of Mg substituted Ni–Cu ferrites," *Journal of Magnetism and Magnetic Materials*, vol. 324, no. 16, pp. 2506–2511, 2012.

[21] K. P. Priyanka, S. Joseph, S. Thankachan, E. M. Mohammed, and T. Varghese, "Effect of electron beam irradiation on optical properties of manganese tungstate nanoparticles," *Journal of Nanotechnology*, vol. 2013, Article ID 580308, 6 pages, 2013.

[22] K. Shreekrishna, U. Kumar, and B. S. N. Sarma, "Design, development, and analysis of thin film coated coir fibre for electronic and industrial applications," *Cer*, vol. 7, pp. 81–91, 2011.

[23] A. Prasad and A. Basu, "Dielectric and impedance properties of sintered magnesium aluminum silicate glass-ceramic," *Journal of Advanced Ceramics*, vol. 2, no. 1, pp. 71–78, 2013.

[24] M. Buchi Suresh and R. Johnson, "Synthesis and high temperature dielectric and complex impedance spectroscopic studies of dense ZnAl$_2$O$_4$ ceramics," *Journal of Materials Engineering and Performance*, vol. 1, pp. 1–8, 2017.

[25] D. Rao and S. Asthana, "The impedance and conductivity studies on BiFeO$_3$ and 0.90BiFeO$_3$-0.10Bi$_{0.5}$Na$_{0.5}$TiO$_3$ ceramics," *AIP Conference Proceedings*, vol. 1663, 2015.

[26] B. Kaur, V. Lakbir Singh, A. Reddy, D.-Y. Jeong, N. Dabra, and J. S. Hundal, "AC impedance spectroscopy, conductivity, and optical studies of Sr doped bismuth ferrite nanocomposites," *International Journal of Electrochemical Science*, vol. 11, pp. 4120–4135, 2016.

[27] R. M. Al-Haddad, I. M. Ali, I. M. Ibrahim, and I. M. Al-Essa, "DC and AC conductivity measurements of Se$_{60}$Te$_{30}$Ge$_{10}$ films," *Al-Nahrain Journal of Science*, vol. 12, no. 4, pp. 72–77, 2009.

[28] C. Cheng, W. Cao, S. Huang et al., "Oxygen-vacancy-ordering-induced metal-insulator transition in MgO single crystals," *Results in Physics*, vol. 36, article 105452, 2022.

[29] B. Véliz, A. Orpella, and S. Bermejo, "Capacitance study of a polystyrene nanoparticle capacitor using impedance spectroscopy," *Nanotech*, vol. 30, no. 40, article 405702, 2019.

[30] P. Liu, C. Sun, G. Liu, Z. Jiang, and H. Zhao, "Ultra-small-sized multi-element metal oxide nanofibers: an efficient electrocatalyst for hydrogen evolution," *Nanoscale Adv*, vol. 4, no. 7, pp. 1758–1769, 2022.

[31] A. B. J. Kharrata, S. Moussa, N. Moutiaab, K. Khirounib, and W. Boujelbena, "Structural, electrical and dielectric properties of Bi-doped Pr$_{0.8-x}$Bi$_x$Sr$_{0.2}$MnO$_3$ manganite oxides prepared by sol-gel process," *Journal of Alloys and Compounds*, vol. 724, pp. 389–399, 2017.

[32] M. H. Khan and S. Pal, "Frequency and Temperature Dependent impedance study in 50% BaTiO$_3$- 50% La$_{0.7}$Sr$_{0.3}$MnO$_3$ nanocomposite," *Advanced Materials Letters*, vol. 5, no. 7, pp. 384–388, 2014.

[33] L. M. Housel, C. D. Quilty, A. Abraham et al., "Investigation of conductivity and ionic transport of $VO_2(M)$ and $VO_2(R)$ via electrochemical study," *Chemistry of Materials*, vol. 30, no. 21, pp. 7535–7544, 2018.

[34] S. Halder, M. S. Sheikh, B. Ghosh, and T. P. Sinha, "Electronic structure and electrical conduction by polaron hopping mechanism in A_2LuTaO_6 (A= Ba, Sr, Ca) Double Perovskite Oxides," *Ceramics International*, vol. 43, no. 14, pp. 11097–11108, 2017.

[35] P. Manimuthu, M. N. J. G. Mariam, R. Murugaraj, and C. Venkateswaran, "Metal-like to insulator transition in $Lu_3Fe_5O_{12}$," *Physics Letters A*, vol. 378, no. 20, pp. 1402–1406, 2014.

[36] S. Pandey, D. Kumar, O. Prakash, and L. Pandey, "Impedance spectroscopy: a powerful technique for the study of electronic ceramics," in *Ceramic Materials - Synthesis, Characterization, Applications and Recycling*, Intechopen Book series, 2019.

[37] R. Jacob, H. G. Nair, and J. Isac, "Impedance spectroscopy and dielectric studies of nanocrystalline iron doped barium strontium titanate ceramics," *Processing and Application of Ceramics*, vol. 9, no. 2, pp. 73–79, 2015.

[38] S. K. Barik, R. N. P. Choudhary, and A. K. Singh, "Ac impedance spectroscopy and conductivity studies of $Ba_{0.8}Sr_{0.2}TiO_3$ ceramics," *Advanced Materials Letters*, vol. 2, no. 6, pp. 419–424, 2011.

[39] K. L. L. Maldonado, P. de la Presa, M. A. de la Rubia et al., "Effects ofgrain boundary width and crystallite size on conductivity and magnetic properties of magnetite nanoparticles," *Journal of Nanoparticle Research*, vol. 16, no. 7, 2014.

[40] H. S. Magar, R. Y. A. Hassan, and A. Mulchandani, "Electrochemical impedance spectroscopy (EIS): principles, construction, and biosensing applications," *Sensors*, vol. 21, no. 19, p. 6578, 2021.

[41] A. K. Roy, K. Prasad, and A. Prasad, "Piezoelectric, impedance, electric modulus and AC conductivity studies on $(Bi_{0.5}Na_{0.5})_{0.95}Ba_{0.05}TiO_3$," *Processing and Application of Ceramics*, vol. 7, no. 2, pp. 781–791, 2013.

[42] R. Tang, C. Jiang, W. Qian et al., "Dielectric relaxation, resonance and scaling behaviors in $Sr_3Co_2Fe_{24}O_{41}$ hexaferrite," *Scientific Reports*, vol. 5, no. 13645, pp. 1–11, 2015.

[43] J. Hou and R. V. Kumar, "B-site multi-element doping effect on electrical properties of bismuth titanate ceramics," pp. 242–274, 2011, http://Intechopen.com/books/ferroelectrics-physicaleffects.